PAPER

Axisymmetric benchmarks of impurity dynamics in extended-magnetohydrodynamic simulations

View the article online for updates and enhancements.

Axisymmetric benchmarks of impurity dynamics in extended-magnetohydrodynamic simulations

B C Lyons[1] , **C C Kim[2]**, **Y Q Liu[1]**, **N M Ferraro[3]**, **S C Jardin[3]**,
J McClenaghan[1], **P B Parks[1]** and **L L Lao[1]**

[1] General Atomics, San Diego, CA 92121, United States of America
[2] SLS2 Consulting, San Diego, CA 92107, United States of America
[3] Princeton Plasma Physics Laboratory, Princeton, NJ 08543-0451, United States of America

E-mail: lyonsbc@fusion.gat.com

CrossMark

Abstract

A verification benchmark has been carried out between the M3D-C1 and NIMROD extended-magnetohydrodynamic codes for simulations of impurity-induced disruption mitigation. Disruptions are a significant concern for future tokamaks and high-fidelity simulations are required in order to ensure the success of disruption mitigation techniques (e.g. shattered-pellet injection) in large-scale fusion reactors. Both magnetohydrodynamic (MHD) codes have been coupled to the Killer Pellet RADiation code for impurity dynamics. The codes show excellent agreement in four axisymmetric, nonlinear simulations, particularly during the thermal quench. This agreement is seen in the time histories of global plasma quantities such as thermal energy, radiated power, and total number of electrons, as well as 2D contours of temperature and current density. The simulations predict that, given the same number of atoms injected, argon quenches the plasma two-to-three times as fast as neon. Furthermore, the inclusion of temperature-dependent Spitzer resistivity causes the current to diffuse and to decay, inducing axisymmetric MHD instabilities that result in a current quench. This work represents an important verification of the coupled impurity and MHD models implemented in M3D-C1 and NIMROD, giving greater confidence in the ability of both codes to perform more sophisticated disruption mitigation simulations.

Keywords: magnetohydrodynamics, impurities, disruptions, disruption mitigation, integrated modeling, benchmark

(Some figures may appear in colour only in the online journal)

1. Introduction

Disruptions pose a significant risk to future tokamak reactors [1, 2]. The rapid, uncontrolled loss of plasma confinement may melt plasma-facing components (PFCs) and exert potentially damaging electromagnetic forces on external structures. Furthermore, disrupting plasmas are capable of generating high-energy beams of runaway electrons, which may damage both PFCs and components behind the first wall. Due to the cost and difficulty of repairing such damage in irradiated, reactor-scale tokamaks, experimental and theoretical capabilities for predicting and avoiding disruptions must be developed [2]. Nevertheless, it is anticipated that it will be challenging to operate tokamaks completely disruption-free. Thus, effective means of mitigating unavoidable disruptions are required.

The most promising methods of disruption mitigation involve the injection of large amounts of impurities into the tokamak as soon as an imminent disruption is detected. These impurities quickly dissipate the stored thermal energy of the plasma through ionization and radiation. This 'thermal quench' increases the resistivity of the plasma, which in turn

1

induces the rapid loss of the plasma current ('current quench'). An effective disruption mitigation system based on these techniques would evenly distribute the radiated power over the first wall, greatly decreasing the heat flux to the PFCs. Ideally, the time scales of the thermal and current quenches would be fast enough to dissipate the energy before a disruptive instability occurs, but slow enough so as not to produce runaway electrons or significant electromagnetic impulses on the device [2, 3].

Several disruption mitigation systems have been tested experimentally, including massive gas injection [4–9] (MGI), shattered-pellet injection [10, 11] (SPI), and shell-pellet injection [12, 13]. All three of these techniques have been shown to mitigate disruptions on contemporary tokamaks effectively. Nevertheless, the projection of these systems to future tokamaks, such as ITER, requires advanced theoretical and numerical models. The workhorses of such research are 3D magnetohydrodynamic (MHD) codes, such as NIMROD [14, 15], M3D-C1 [16], and JOREK [17, 18], which are capable of simulating the time evolution of a disrupting tokamak plasma. These codes typically simulate plasmas as consisting of one or two fluids (electrons and a single ion species). In order to model disruption mitigation, these MHD codes must be coupled to appropriate models for impurity species, including ionization, radiation, and transport.

NIMROD, coupled to the Killer Pellet RADiation (KPRAD) coronal model for impurity dynamics, has already been used to study MGI extensively [19–22]. Such simulations, however, showed that the technique would project poorly to a reactor-scale device and are, in part, responsible for the abandonment of MGI in ITER [21, 22]. Instead, the present plan is for ITER to use SPI as its primary mitigation technique, though there are many outstanding questions as to the best design and operation of this system.

Given the utmost importance in developing an effective disruption mitigation system, it is essential that the tools being used to make such predictions are of the highest fidelity. Recently, M3D-C1 has been coupled to the KPRAD code as well [23], using similar, though not identical methods as found in NIMROD. This provides an excellent opportunity to verify the models. Here, we present a detailed benchmark between NIMROD and M3D-C1 coupled MHD-impurity, nonlinear simulations in axisymmetric geometries. These simulations are the first in an extensive set of planned verification and validation studies. While this initial study neglects 3D instabilities relevant to disruption dynamics, we are able to explore both impurity and MHD physics that are important in the thermal quench and early current quench dynamics, during which the plasma may remain largely axisymmetric. In addition, these simulations are relatively computationally inexpensive, using $O(10^3)$ cpu-hours compared to $O(10^5)$ cpu-hours for 3D, nonlinear simulations.

Section 2 provides an overview of KPRAD, M3D-C1, and NIMROD. Details on cases considered in the benchmark can be found in section 3. Section 4 examines detailed time histories of key plasma quantities in both codes, while a comparison of detailed dynamics for one of the benchmark cases is considered in section 5. Finally, we summarize these results in section 6, as well as discuss plans for future benchmarks and predictive modeling.

2. Overview of models

2.1. KPRAD impurity model

The KPRAD code was originally developed to model the deposition and evolution of pellet material in a plasma [24]. We make use of a version of the code containing just the impurity dynamics. This implements a coronal model for impurity ionization, recombination, and radiation (from line, bremsstrahlung, and recombination), which is valid for low-density plasmas in which the rate of spontaneous decay of excited ions is significantly higher than the rate of collisional de-excitation. The ionization, recombination, and radiation rates are determined by a polynomial fit to data within the ADPAK atomic database [25], allowing for efficient and accurate calculations. The model has been implemented for helium, beryllium, carbon, neon, and argon.

2.2. M3D-C1 coupling

M3D-C1 solves the 3D, nonlinear, two-fluid extended-MHD equations in toroidal geometries [16]. It uses fourth-order, C^1-continuous finite elements on an unstructured triangular mesh in the poloidal plane along with third-order, cubic-Hermite finite elements (also C^1 continuous) in the toroidal direction. While the toroidal mesh is structured, each poloidal plane can be placed at an arbitrary toroidal location, allowing for packing in the toroidal angle.

KPRAD has now been tightly-coupled to M3D-C1 for single-fluid simulations, meaning that a single plasma velocity (same for electrons and all ion species) is advanced by a momentum equation, which has been summed over all charged species. Each species, however, has its own density continuity equation. The ionization and recombination rates from KPRAD provide sources that couple the various continuity equations together, accounting for the change in electron and impurity charge-state densities. In addition, four different models for the temperature evolution were implemented:

- single, total pressure equation (p_e/p fixed),
- single temperature equation (summed over all species, T_e/T_i fixed),
- two pressure equations (one for total and one for electron),
- and two temperature equations (one for electrons and one summed over all ions).

In all cases, all ion species are assumed to have the same temperature. KPRAD also provides an energy loss term in the the pressure/temperature equation(s) due to ionization and radiation (line, Bremsstrahlung, and recombination). For the models with a single pressure/temperature equation, this results in energy loss from the electrons and all ion species. For the two-equation

models, the KPRAD losses are only coupled to the electron equation and energy is lost from ions by classical thermal equilibration with the cooling electrons. Note that the recombination radiation energy consists of two components, namely the kinetic energy of the captured electron and the potential energy between the electron and the capturing ion. The former is subtracted from the plasma's thermal energy. The latter is not, as this potential energy is built up during ionization and has already been removed from plasma's thermal energy.

The coupling between KPRAD and M3D-C1 is implemented by splitting each time step into three parts. In the first, KPRAD is sub-cycled on an adaptive time step to calculate the evolution of the impurity charge states, along with the total ionization and radiation power over the course of a full MHD time step. In the second part, the M3D-C1 MHD equations are advanced, including appropriate sources from KPRAD. Finally, the impurities are advected using the newly calculated, MHD single-fluid velocity. Equations for this implementation can be found in appendix and further details in [23].

2.3. NIMROD coupling

NIMROD is a 3D, initial-value simulation code that solves the extended-MHD equations. NIMROD utilizes 2D, quadrilateral, high-order finite elements in the poloidal plane and a finite Fourier series in the toroidal angle. Advanced implicit and semi-implicit time-stepping algorithms are used to evolve the equations. Details on the full set of equations and algorithms can be found in [14] and [15].

To model the thermal quench, NIMROD assumes a single-fluid picture of the plasma where all species share a single temperature and are advected by the same velocity. Each impurity charge-state density is advanced along with the ion density. The electron density is computed by enforcing quasi-neutrality. A temperature equation summed over all species is advanced, as in the single temperature equation model in M3D-C1. NIMROD also uses the KPRAD subroutines for the ionization and radiation modeling and a similar multi-step coupling where the faster KPRAD subroutines are sub-cycled using the fast and accurate integrator LSODE [26]. Details for these equations can be found in appendix.

In addition to the impurity model presented above, NIMROD has the additional option of including a deuterium mixture with the impurities. With this option, we include the neutral density of both deuterium (assumed to be the background plasma species) and neutral impurities when defining the plasma mass density and number density. Both neutral densities are also advanced using the single-fluid velocity and temperature. Also included with this option is three-body recombination [27], which becomes dominant at very low temperatures of a few eV. Although not essential for the thermal quench, resolving the neutral dynamics will be important for current quench simulations and runaway-electron modeling.

3. Benchmark setup

To test the coupling to KPRAD, several cases were run by both extended-MHD codes, all based on variations of the same problem. We began with an equilibrium reconstruction of DIII-D shot 137611 at 1950 ms, an equilibrium used in previously published NIMROD simulations of disruption mitigation [20, 28]. To start, a pure-deuterium plasma was assumed with spatially uniform ion and electron density, $n_i = n_e = 1 \times 10^{20}$ m^{-3}. Both codes were run using a single temperature equation model with a single temperature for electrons and all ion species. All simulations discussed in the following sections are 2D (axisymmetric) and nonlinear. Generally, constant diffusivities were used in the domain. In particular, the isotropic density diffusivity was set to 10 m^2 s^{-1}, the isotropic momentum and perpendicular thermal diffusivities were both set to 100 m^2 s^{-1}, and the parallel thermal diffusivity was set to 1×10^8 m^2 s^{-1}. Both codes were run using a fixed, superconducting boundary with no resistive wall. Details of the equilibrium and simulation domain can be found in figure 1.

An axisymmetric, Gaussian, neutral impurity-density source was implemented such that

$$\sigma_{z,0}^{src} = \nu \frac{R_0}{R} \exp\left(-\frac{(R - R_0)^2 + (Z - Z_0)^2}{2\delta^2}\right), \qquad (1)$$

where ν is a constant injection rate set equal to 1×10^{23} m^{-3} s^{-1}, R and Z are the major-radius and height coordinates, $(R_0, Z_0) = (1.77037$ m, 0.01447 m$)$ is the location of the magnetic axis, and the half-width of the Gaussian is $\delta = 0.25$ m. Contours of this source can be found in figure 1. Integrating over the whole domain, the total number of impurity ions injected is approximately 4.37×10^{23} per second. This is on the order of the particle content of a millimeter neon or argon pellet every millisecond. Such an impurity source can be considered the idealized result of a disruption mitigation system optimized to reduce nonaxisymmetric MHD modes and the radiative toroidal peaking factor (e.g. by pellet injection at multiple toroidal angles) and for core deposition of impurities (e.g. by shell-pellet injection).

Four cases were considered in this benchmark, namely, the injection of either argon or neon with either constant or Spitzer resistivity. In the constant resistivity simulations, η was fixed to 1×10^{-5} Ωm. Note that in the M3D-C1 simulations, to ensure numerical stability, the resistivity was artificially increased far outside the separatrix; this did not appear to impact the physical evolution of the core plasma. In the Spitzer resistivity calculations, we took $\eta = Z_{eff} \eta_0 (T_0/T_e)^{3/2}$, where Z_{eff} is the local, effective charge number of the plasma, T_e is the electron temperature, and $\eta_0 = 1.83339 \times 10^{-8}$ Ωm is the initial, on-axis resistivity, corresponding to an initial, on-axis temperature of $T_0 = 3794.26$ eV. Note that these values of η_0 and T_0 result in an enhanced Spitzer resistivity approximately 2.444 times higher than the physical Spitzer resistivity. In addition, to prevent numerical instabilities between the ohmic heating and radiative cooling, both codes imposed a maximum resistivity of
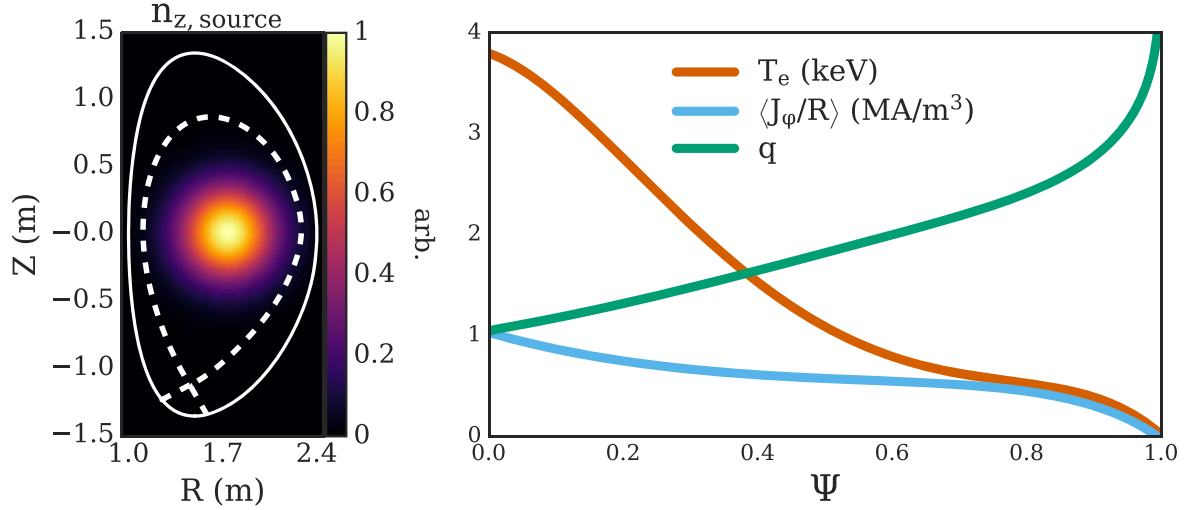
Figure 1. Details of the equilibrium and benchmark. Left: normalized impurity source distribution with the simulation domain (solid white) and original last-closed flux surface (dashed white) overlaid. Right: initial temperature, current, and safety factor profiles of the equilibrium. Note that we assume a spatially uniform initial density, though the experimental density is nonuniform. The temperature is then determined by self-consistency with the experimental pressure profile.
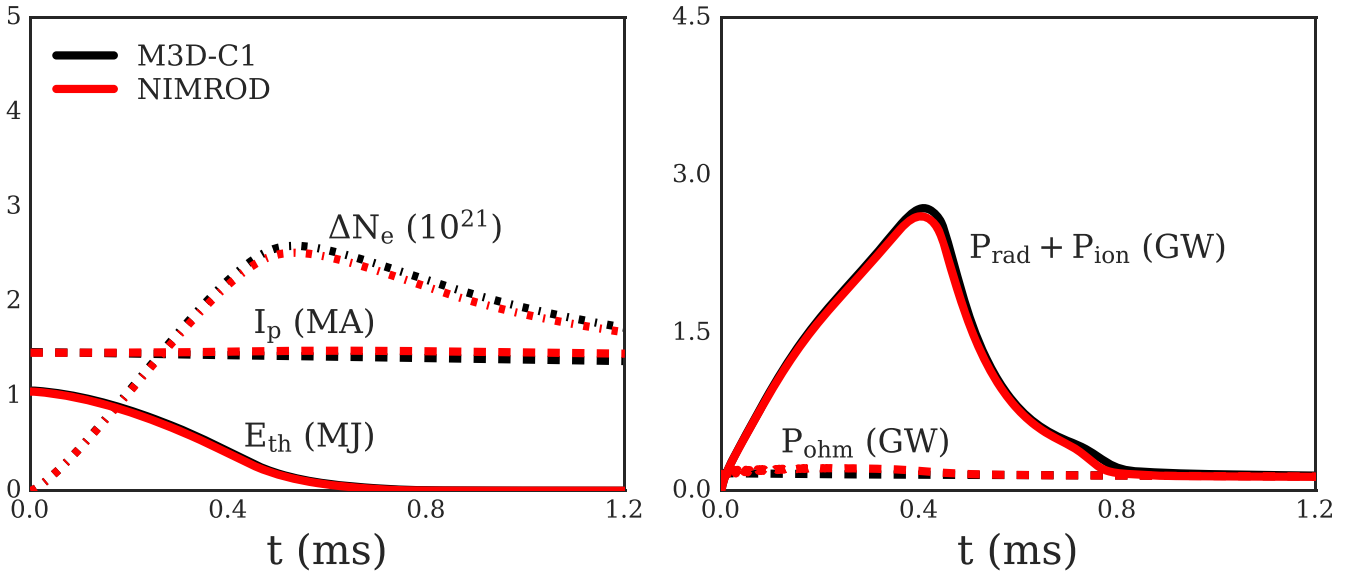
Figure 2. For argon injection with constant resistivity, time histories of important 0D plasma quantities. Left: thermal energy, plasma current, and change in electron number. Right: KPRAD loss power (radiation plus ionization) and ohmic heating power.

0.0484525 Ωm, which would correspond to a temperature of 0.198491 eV.

power (P_{ohm}). Each of these quantities is examined in detail for each benchmark case in the following sections.

## 4. Time evolution of thermal quench

In all four cases considered, excellent agreement is found between the M3D-C1 and NIMROD simulations, particularly during the thermal quench (i.e. the rapid loss of thermal energy). This agreement is readily seen in time histories of the thermal energy (E_{th}), plasma current (I_p), change in the total number of electrons (ΔN_e), as well as the KPRAD loss power (radiation [P_{rad}] and ionization [P_{ion}]) and the ohmic heating

4.1. Argon injection with constant resistivity

The time histories for the first case of argon injection with constant resistivity are shown in figure 2. The evolution of the thermal quench is found to be nearly identical between the two codes. As the argon is injected, the electron number and loss power rise nearly linearly, while the thermal energy drops, at first slowly, and then more rapidly. Between 0.40 and 0.41 ms, the loss power reaches a maximum as the temperature in the core drops, falling below 10 eV at 0.45 ms. At this point, the ionization rate in the plasma decreases and recombination increases, causing
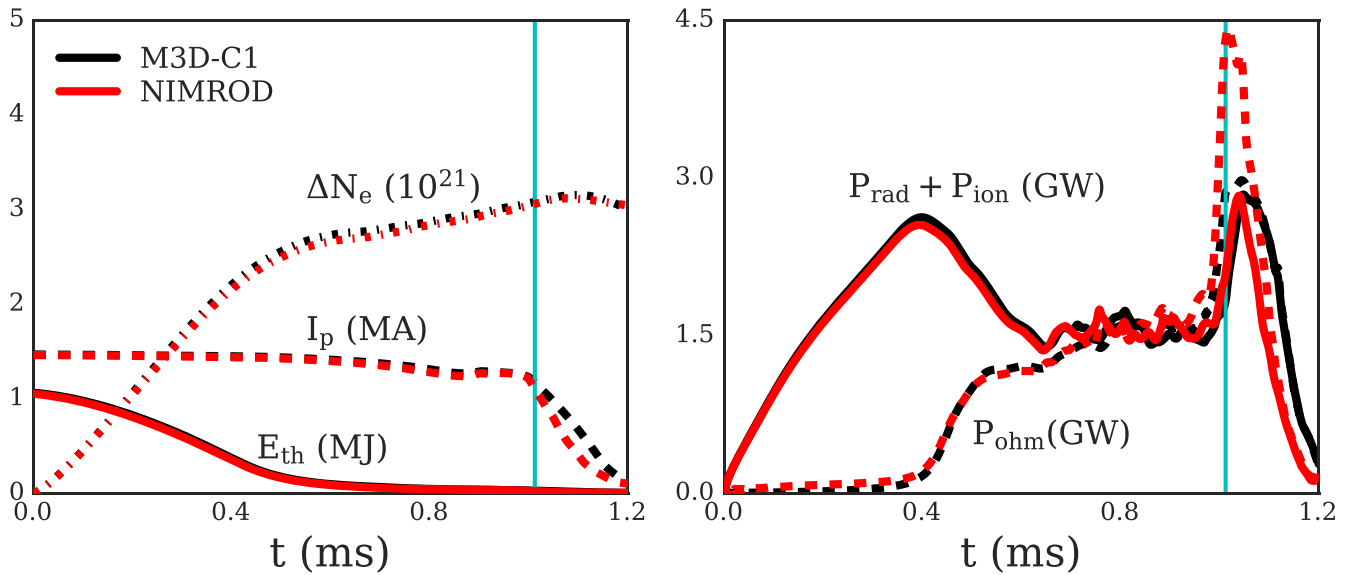
Figure 3. For argon injection with Spitzer resistivity, time histories of important 0D plasma quantities. Left: thermal energy, plasma current, and change in electron number. Right: KPRAD loss power (radiation plus ionization) and ohmic heating power. The vertical cyan line denotes when the plasma makes contact with the domain boundary.

the electron number to begin falling at 0.53 ms. The loss power continues to fall until it reaches the level of the ohmic heating, which remains roughly constant in the simulation due to the constant, low resistivity. 99% of the plasma thermal energy is lost by 0.73 ms in the NIMROD run and 0.76 ms in the M3D-C1 run. The plasma current, however, decays less than 10% throughout the simulations.

4.2. Argon injection with Spitzer resistivity

Figure 3 shows the time histories for argon injection with Spitzer resistivity, demonstrating excellent agreement between the two codes. The initial behavior of these runs is very similar to the case with constant resistivity. The loss power peaks slightly earlier, between 0.39 and 0.40 ms, which is followed by the temperature on-axis falling below 10 eV at 0.46 ms. At this point, however, the low temperature in the core causes the resistivity to rise dramatically; as a result, the current decay rate and ohmic power also rise between 0.4 and 0.5 ms. This additional heating raises the minimum temperature within the simulations compared to the constant resistivity case, creating a tail in the thermal energy dissipation. Furthermore, this higher temperature allows ionization to continue and the electron number to rise (albeit at a slower rate).

The loss power comes into balance with the ohmic heating between 0.72 and 0.76 ms, at which point the poloidal magnetic energy is being converted to thermal energy and then quickly radiated away. After this occurs, there are some quantitative differences in the ohmic and loss powers between the two codes. As will be discussed in section 5, there exists $n = 0$ MHD turbulence in the core at this point in the simulations, making it unlikely that the two codes would agree exactly. Nevertheless, the qualitative nature of these dynamics is found to agree remarkably well. As will also be shown in section 5, the plasma becomes $n = 0$ unstable and rapid loss of current occurs once the plasma makes contact with the domain boundary,

demonstrating a current quench. Beyond some broad, qualitative features, however, the axisymmetric nature of the simulations and the idealized boundary conditions mean that these current quench dynamics are not physically realistic.
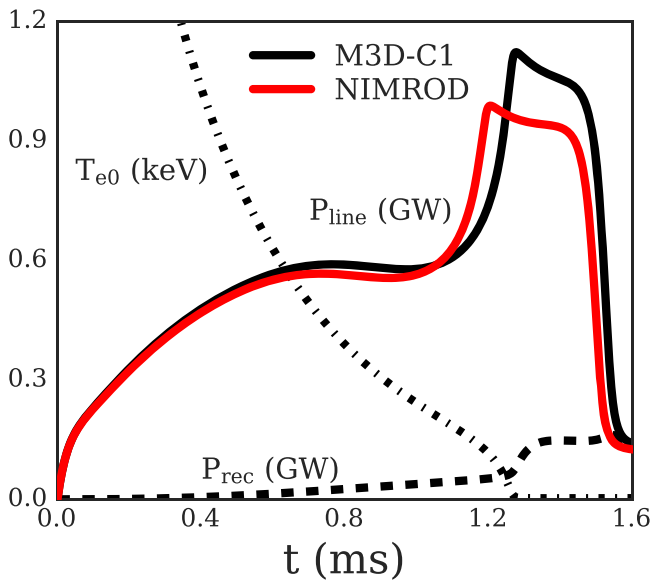
4.3. Neon injection with constant resistivity

Both M3D-C1 and NIMROD also found general, quantitative agreement in their simulation of a quench induced by neon with constant resistivity, as seen in figure 4. The thermal quench occurs nearly three times more slowly as compared to the argon-induced quench of section 4.1. The loss power does not peak until 1.20 ms in NIMROD and 1.28 ms in M3D-C1. Likewise, the electron number does not reach a maximum until 1.37 ms in NIMROD and 1.39 ms in M3D-C1. This slower timescale is due to the lower atomic number of neon (10 versus 18 for argon), which results in lower ionization and radiation powers, along with a slower increase in the electron number. In fact, the loss power appears to level off between 0.4 and 1.0 ms, presumably due to an offset between the rising electron and impurity densities, which increase radiation and ionization, and the falling temperature, which decreases them. As the plasma retains a higher temperature during the slower, neon-induced thermal quench, ionization continues for a longer period of time, resulting in significantly higher electron numbers as compared to the argon-induced quenches.

After 1.0 ms, both codes show a rapid increase in the loss power before it levels off once again at a higher value. As can be seen in figure 5, this increase is due to a rise in line radiation, associated with a rapid collapse of the temperature on-axis from O(100) eV to O(1) eV. This indicates the existence of strong line resonances in this temperature range. Once the temperature on-axis falls below ~10 eV, the recombination radiation increases significantly, indicating
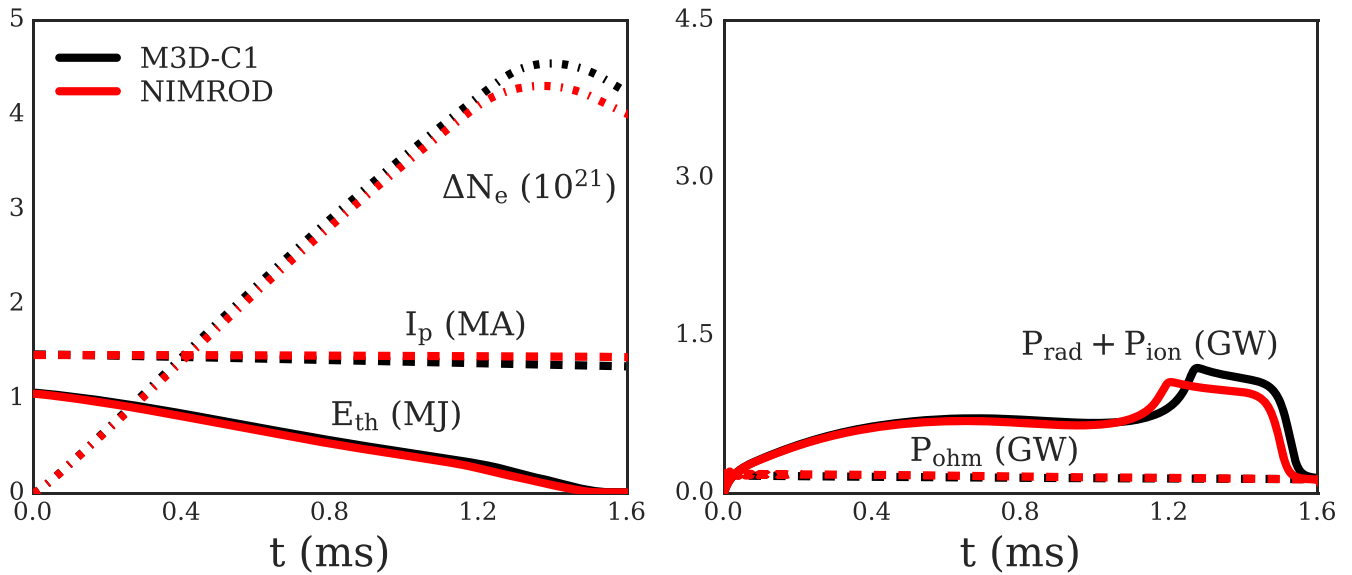
Figure 4. For neon injection with constant resistivity, time histories of important, global plasma quantities. Left: thermal energy, plasma current, and change in electron number. Right: KPRAD loss power (radiation plus ionization) and ohmic heating power.

Figure 5. For neon injection with constant resistivity, time histories of the line radiation (P_{line}), for both M3D-C1 and NIMROD, and the recombination radiation power (P_{rec}) and on-axis electron temperature (T_{e0}) from M3D-C1. Note that the majority of the recombination radiation comes from the plasma's potential energy, which does not reduce the plasma thermal energy.

that recombination is becoming the dominant process in the plasma core.

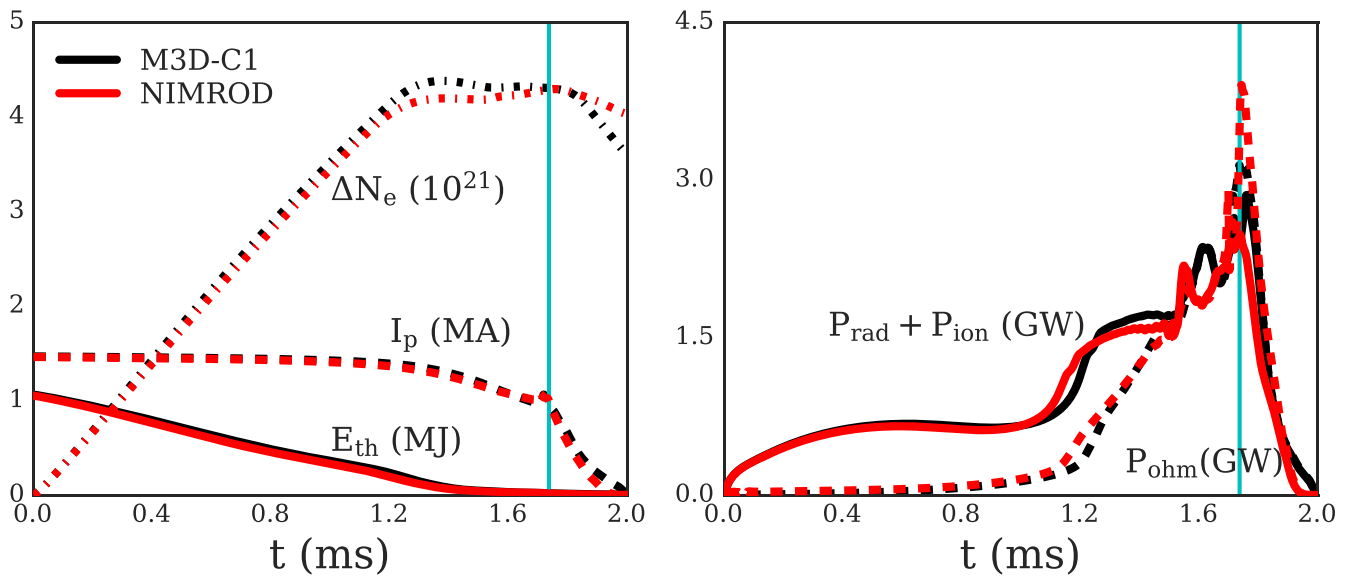### 4.4. Neon injection with Spitzer resistivity

Finally, as shown in figure 6, M3D-C1 and NIMROD also show general quantitative agreement for the case of neon injection with Spitzer resistivity. The thermal quench time scales are roughly similar to those in the case of neon injection with constant resistivity, quenching the plasma about two-to-three times as slowly as argon. As occurred in the

argon simulations with Spitzer resistivity, the ohmic heating increases substantially (between 1.1 and 1.5 ms) as the temperature in the core drops. Around 1.5 ms, the ohmic power comes into balance with the loss power. Between 1.5 and 1.7 ms, MHD turbulence once again lead to oscillations in the loss power and ohmic heating, and contact with the domain boundary after 1.7 ms leads to a rapid current quench. During these phases, there are some quantitative discrepancies, while excellent qualitative agreement between the codes is maintained.

5. Detailed dynamics of thermal and current quench

In order to illustrate some of the detailed dynamics of these impurity-induced thermal and current quenches, we have plotted 2D contours of the electron temperature (figure 7) and toroidal current density (figure 8) for the case of argon injection with Spitzer resistivity (see section 4.2). Four times were chosen: 0.35 ms (just before peak radiation), 0.55 ms (just after the rise in ohmic heating), 0.9 ms (ohmic heating balances loss powers), and 1.1 ms (into rapid current quench). For the first three times, these contours demonstrate excellent agreement between M3D-C1 and NIMROD. At the final time, the codes agree in certain qualitative features, but differ quantitatively.

Comparing the temperatures between 0.35 and 0.55 ms, we see an 'inside-out' thermal quench, qualitatively similar to the expected effect of successful shell-pellet mitigation [29]. The temperature on-axis collapses to O(1) eV but a shell of O(100) eV plasma remains exterior to this. The drop on-axis, however, corresponds to the falling loss power and rising ohmic heating found in figure 3. A very steep temperature gradient forms, leading to $n = 0$ instabilities, as seen by the turbulent eddies originating from the outboard midplane and shooting toward the core at 0.55 and 0.9 ms in figure 7. The

Figure 6. For neon injection with Spitzer resistivity, time histories of important, global plasma quantities. Left: thermal energy, plasma current, and change in electron number. Right: KPRAD loss power (radiation plus ionization) and ohmic heating power. The vertical cyan line denotes when the plasma makes contact with the domain boundary.
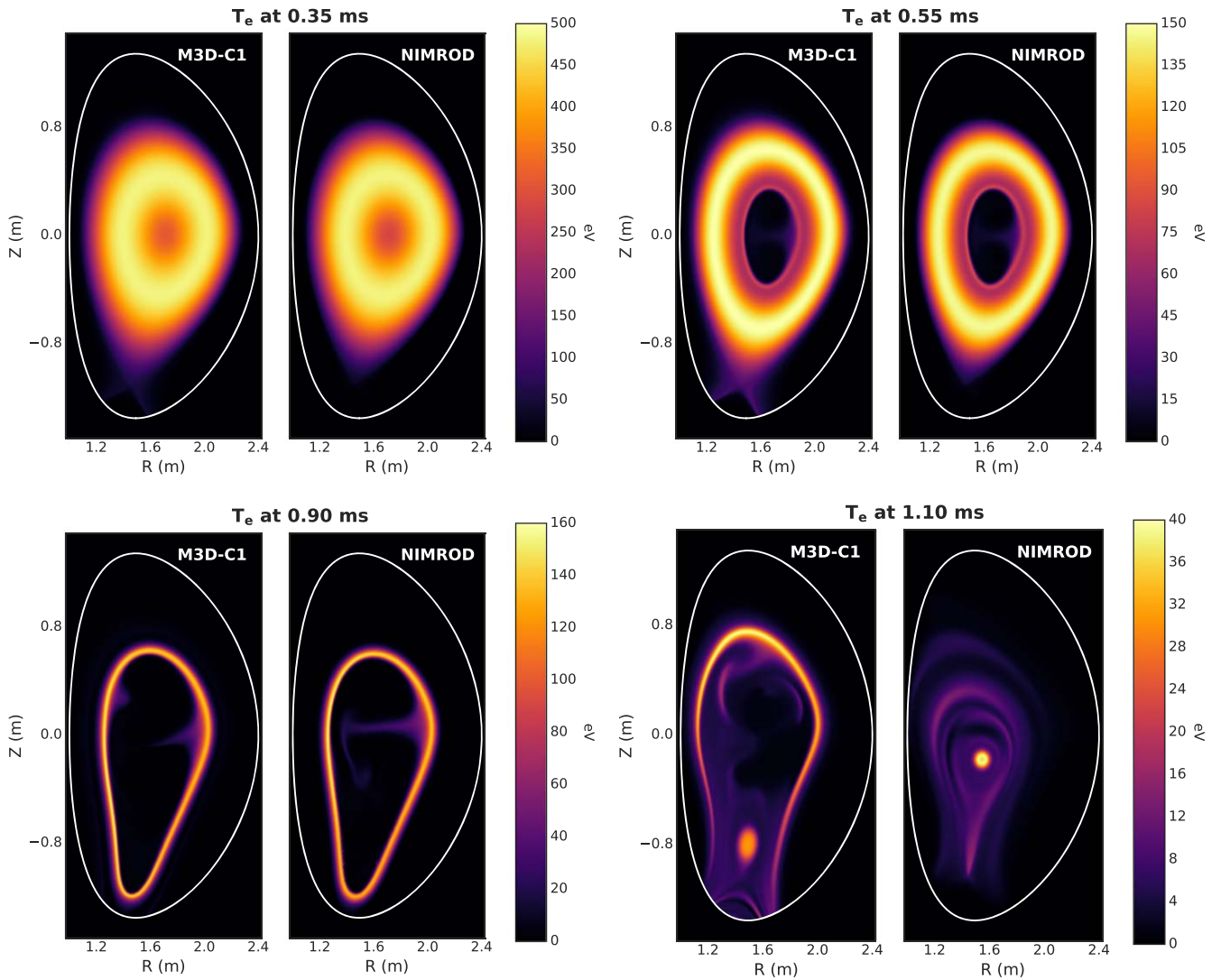
Figure 7. Electron temperatures throughout the argon-induced quench with Spitzer resistivity, showing an inside-out thermal quench. Note that the color scale varies at each time.
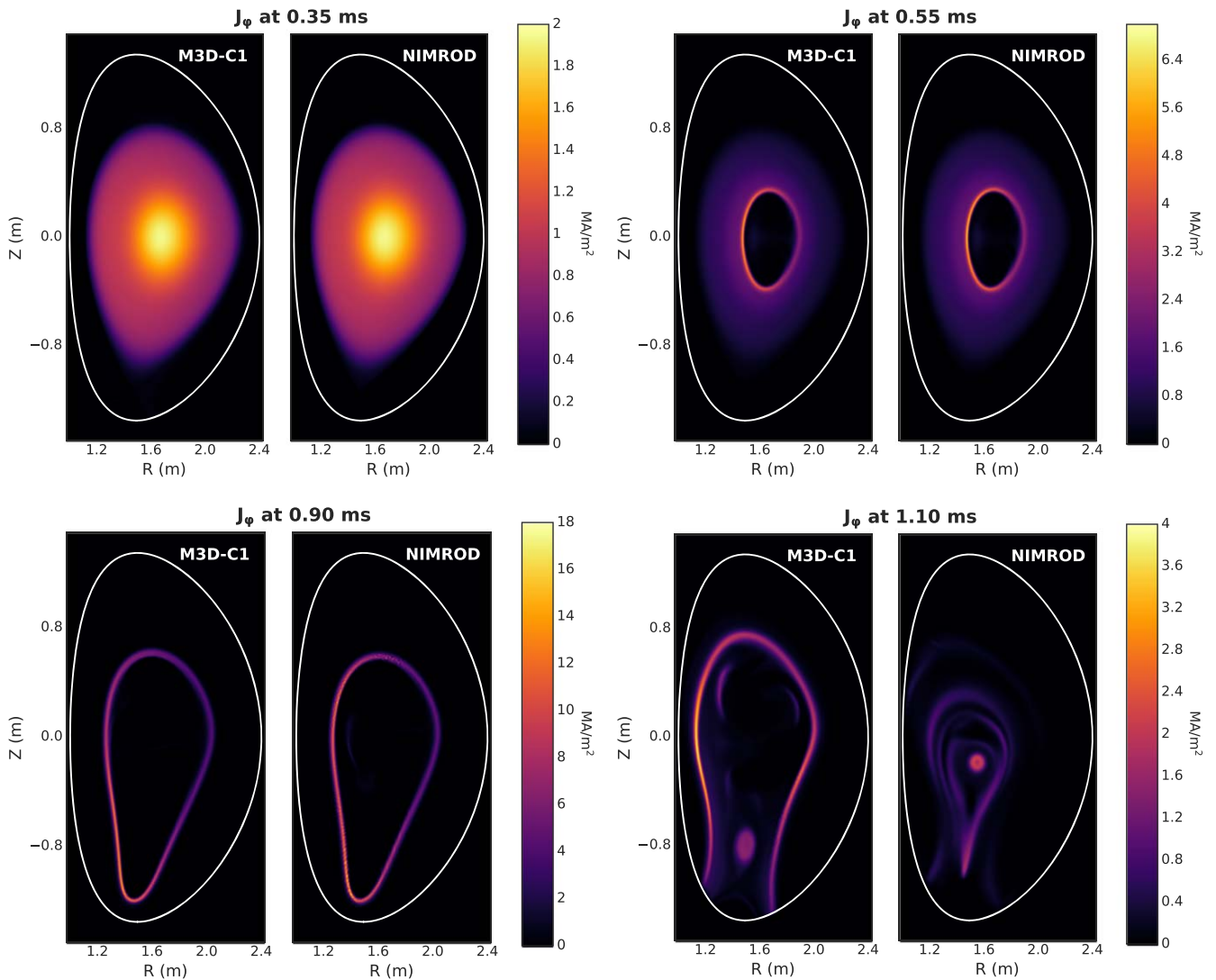
Figure 8. Toroidal current density throughout the argon-induced quench with Spitzer resistivity, showing the creation of a hollow current profile. Note that the color scale varies at each time.

exact details of these turbulent dynamics do vary between the codes, accounting for the quantitative differences in the loss power and ohmic heating found in figure 3 between 0.7 and 1.0 ms. As seen in figure 8 at those two intermediate times, the low temperature (and, therefore, high resistivity) in the core forces the current to diffuse outward. The plasma current gets concentrated in a current sheet which gradually expands outward, subject to electromagnetic forces. All the ohmic power, therefore, is concentrated in this current sheet, leading to a similar sheet of warm, O(100) eV plasma. It is within this sheet of current and warm plasma that most of the ionization, radiation, and ohmic heating occurs from roughly 0.7–0.9 ms.

This current sheet is unstable to $n = 0$ and the lower half of the plasma gets pulled down toward the domain boundary. At approximately 1.0 ms, the current sheet makes contact with the simulation boundary, causing the current to decay rapidly and the ohmic heating to spike in both codes. In M3D-C1, however, the loss power spikes as well, while it remains rather constant in the NIMROD simulations. In M3D-C1, a current

sheet remains that appears to be attached to the boundary. In NIMROD, however, the sheet largely disappears. Despite these differences, certain qualitative features are observed in both codes. The plasma rapidly cools to just O(10) eV in isolated locations. In addition, both codes show the creation of a concentrated current filament, though this is significantly stronger in the NIMROD calculations.

The exact details of these late-time dynamics are no doubt strongly influenced by the boundary conditions implemented in both codes. In reality, however, this stage of the dynamics would be dominated by interactions with a resistive wall that is not present in our fixed-boundary simulations. Furthermore, the steep gradients in both pressure and current that arose in these simulations are an artifact of enforced axisymmetry and ought to drive 3D MHD instabilities, such as interchange and kink modes. Past research has shown that similar current sheets are indeed unstable to 3D modes [23, 30, 31]. Both M3D-C1 and NIMROD are capable of modeling such resistive wall and 3D

dynamics. A detailed verification of these late-time dynamics is therefore reserved for a non-axisymmetric benchmark, which will be the subject of near-term future work.

6. Conclusion

We have successfully benchmarked the coupling of the KPRAD impurity model to the M3D-C1 and NIMROD extended-MHD codes in axisymmetric geometries. Excellent agreement was found between the two codes when modeling rapid thermal quenches induced by both argon and neon injection and using two different resistivity models. This agreement was seen in the time evolution of the thermal energy, plasma current, total number of electrons, and radiation, ionization, and ohmic heating powers. Beyond this, the codes were well-matched in their 2D evolution of the temperature and toroidal current density, demonstrating excellent agreement in the MHD models. Argon was found to quench the thermal energy about two-to-three times faster than neon. In addition, the simulations demonstrated that the use of temperature-dependent, Spitzer resistivity dramatically changed the late-time evolution. In particular, a tail was observed in the thermal energy decay as the increased ohmic heating balanced the radiative cooling of the plasma. This also resulted in a hollowing of the current density profile and, eventually, an $n = 0$ instability resulting in a current quench.

The axisymmetric benchmarks presented here serve as a strong verification of the impurity-MHD coupling within both M3D-C1 and NIMROD, giving us confidence in the ability of both codes to perform high-fidelity simulations of disruption mitigation by pellet or MGI. Several other verification studies based upon this case are currently underway, including 3D nonlinear modeling and simulations with a resistive wall boundary, allowing us to test more realistic current quench dynamics. In addition, while the impurity source considered here is idealized, being on-axis, axisymmetric, and stationary, more sophisticated impurity source models have been implemented in both codes. These sources will allow for more realistic modeling of disruption mitigation experiments that require complex source models, including the tracking of multiple, moving impurity sources and the ablation of solid material by the plasma that is needed to simulate shattered-pellet injection. The verification, validation, and improvement of these models is the subject of active, on-going work.

Appendix. MHD and impurity equations

Both M3D-C1 and NIMROD solve a similar set of extended-MHD equations that have been coupled to the KPRAD impurity model. The ion densities are advanced according to continuity equations, namely,

$$\frac{\partial n_s}{\partial t} + \nabla \cdot (n_s \mathbf{v}) = \nabla \cdot (D \nabla n_s) + \sigma_s, \tag{A1}$$

where n_s is the number density of species s, $\mathbf{v}$ is the single-fluid velocity, D is particle diffusion coefficient, and σ_s is the source for each species. For impurities of charge-state z, the source term is

$$\sigma_z = \mathcal{I}_{z-1} n_{z-1} - (\mathcal{I}_z + \mathcal{R}_z) n_z + \mathcal{R}_{z+1} n_{z+1} + \mathcal{S}_z, \tag{A2}$$

where $\mathcal{I}_z$ and $\mathcal{R}_z$ are the KPRAD ionization and recombination rates, which are functions of the local electron density and temperature. In the present work, there is no main ion source ($\sigma_i = 0$), and the external source, $\mathcal{S}_z$, is only non-zero for the neutral impurity ions ($z = 0$). Furthermore, advection and diffusion are not included in the neutral continuity equation. The electron density is determined by enforcing quasi-neutrality with the main and impurity ions.

The single-fluid velocity, $\mathbf{v}$, is determined by solving a momentum equation summed over all charged species:

$$\rho \left(\frac{\partial \mathbf{v}}{\partial t} + \mathbf{v} \cdot \nabla \mathbf{v} \right) = \mathbf{J} \times \mathbf{B} - \nabla p - \nabla \cdot \Pi - \varpi\, \mathbf{v}. \tag{A3}$$

Here, ρ is the mass density, $\mathbf{J}$ is the current density, $\mathbf{B}$ is the magnetic field, p is the total, isotropic pressure, Π is anisotropic pressure tensor (accounting for anomalous viscosity), and ϖ is the total mass source (accounting for momentum conservation as particles are added to the system).

In the work considered here, both codes advance a single temperature equation summed over all charged species:

$$n_{\text{tot}}\left[\frac{\partial T}{\partial t} + \mathbf{v} \cdot \nabla T + (\Gamma - 1)T\nabla \cdot \mathbf{v}\right] + \sigma_{\text{tot}}T$$
$$= (\Gamma - 1)\left[\eta J^2 - \nabla \cdot \mathbf{q}_{\text{tot}} + Q - \Pi: \nabla\mathbf{v} + \frac{1}{2}\varpi\, v^2\right].$$
$$\text{(A4)}$$

This T is the same for all species ($T_e = T_i = T_z = T$). Here 'tot' refers to a sum over all charged species, $\mathbf{q}$ is the heat flux (which includes anisotropic parallel and perpendicular thermal conduction). The heat source, Q, is negative and include ionization and radiation cooling calculated by KPRAD.

These equations are closed by the resistive Ohm's law and Maxwell's equations. Furthermore, both codes allow for some additional optional features. Instead of equation (A4), M3D-C1 can solve a single pressure equation, or two temperature or pressure equations, as mentioned in section 2.2 and explained extensively in [23]. NIMROD has an option for including additional neutral and main ion dynamics, as discussed in section 2.3. When doing so, the neutrals are advected and diffused according to a continuity equation like equation (A1), and ionization and recombination (including three-body) are included for the main ions. NIMROD's momentum and temperature equations are then summed over all species (including neutrals).

ORCID iDs

B C Lyons ⓘ https://orcid.org/0000-0003-3232-1581

References

[1] ITER Physics Expert Group on Disruptions, Plasma Control and MHD and ITER Physics Basis Editors 1999 *Nucl. Fusion* **39** 2251
[2] Hender T C *et al* (The ITPA MHD, Disruption and Magnetic Control Topical Group) 2007 *Nucl. Fusion* **47** S128
[3] Lehnen M *et al* 2015 *J. Nucl. Mater.* **463** 39
[4] Taylor P L *et al* 1999 *Phys. Plasmas* **6** 1872
[5] Bakhtiari M *et al* 2005 *Nucl. Fusion* **45** 318
[6] Granetz R, Whyte D, Izzo V, Biewer T, Reinke M, Terry J, Bader A, Bakhtiari M, Jernigan T and Wurden G 2006 *Nucl. Fusion* **46** 1001
[7] Pautasso G *et al* (the ASDEX Upgrade Team) 2009 *Plasma Phys. Control. Fusion* **51** 124056
[8] Reux C, Bucalossi J, Saint-Laurent F, Gil C, Moreau P and Maget P 2010 *Nucl. Fusion* **50** 095006
[9] Lehnen M *et al* (JET EFDA contributors) 2011 *Nucl. Fusion* **51** 123010
[10] Commaux N, Baylor L, Jernigan T, Hollmann E, Parks P, Humphreys D, Wesley J and Yu J 2010 *Nucl. Fusion* **50** 112001
[11] Commaux N *et al* 2016 *Nucl. Fusion* **56** 046007
[12] Hollmann E M *et al* 2009 *AIP Conf. Proc.* **1161** 65
[13] Hollman E M, Parks P B, Shiraki D, Alexander N, Eidietis N W, Lasnier C J and Moyer R A 2019 *Phys. Rev. Lett.* **122** 065001
[14] Sovinec C R, Glasser A H, Gianakon T A, Barnes D C, Nebel R A, Kruger S E, Schnack D D, Plimpton S J, Tarditi A and Chu M S 2004 *J. Comput. Phys.* **195** 355
[15] Sovinec C and King J 2010 *J. Comput. Phys.* **229** 5803
[16] Jardin S C, Ferraro N, Breslau J and Chen J 2012 *Comput. Sci. Discovery* **5** 014002
[17] Huysmans G and Czarny O 2007 *Nucl. Fusion* **47** 659
[18] Czarny O and Huysmans G 2008 *J. Comput. Phys.* **227** 7423
[19] Izzo V A, Whyte D G, Granetz R S, Parks P B, Hollmann E M, Lao L L and Wesley J C 2008 *Phys. Plasmas* **15** 056109
[20] Izzo V *et al* 2011 *Nucl. Fusion* **51** 063032
[21] Izzo V A 2013 *Phys. Plasmas* **20** 056107
[22] Izzo V *et al* 2015 *Nucl. Fusion* **55** 073032
[23] Ferraro N, Lyons B, Kim C, Liu Y and Jardin S 2019 *Nucl. Fusion* **59** 016001
[24] Whyte D G *et al* 1997 *Proc. 24th European Conf. on Controlled Fusion and Plasma Physics* (Berchtesgaden, Germany) p 1137
[25] Hulse R A 1983 *Nucl. Technol./Fusion* **3** 259
[26] Hindmarsh A C 1980 *ACM SIGNUM Newsletter* **15** 10
[27] Zel'dovich Y B and Raizer Y P 1966 *Physics of Shock Waves and High-Temperature Hydrodynamic Phenomena* (New York: Academic Press) p 407
[28] Izzo V A, Humphreys D A and Kornbluth M 2012 *Plasma Phys. Control. Fusion* **54** 095002
[29] Izzo V A and Parks P B 2017 *Phys. Plasmas* **24** 060705
[30] Ebrahimi F 2016 *Phys. Plasmas* **23** 120705
[31] Ebrahimi F 2017 *Phys. Plasmas* **24** 056119